https://doi.org/10.5194/egusphere-2026-4427
Preprint. Discussion started: 11 August 2026

Characterizing the lower troposphere by combining GNSS radio occultation and nadir sounding observations in a tomographic approach

Kuo-Nung Wang[1], Chi O. Ao[1], George A. Hajj[1], Mary G. Morris[1], and Angelyn W. Moore[1]

[1]Jet Propulsion Laboratory, California Institute of Technology, Pasadena, California, 91109, United States

Correspondence: Kuo-Nung Wang (Kuo-Nung.Wang@jpl.nasa.gov)

Abstract. Characterizing the moist thermodynamic structure of the lower troposphere (LT) from spaceborne observations is challenging. This is largely due to the LT's highly variable moisture distribution which requires high-resolution observations in both the vertical and horizontal dimensions. Two of the most impactful spaceborne remote sensing technologies in numerical weather prediction (NWP) are (1) the global navigation satellite system – radio occultation (GNSS-RO) and (2) nadir sounding instruments which include microwave radiometers (MWR) and infrared sounders (IR). These two technologies provide complementary information of atmospheric temperature and water vapor. GNSS-RO provides high vertical resolution (∼200m) with near zero interference from hydrometeor, but its horizontal resolution along the ray path is coarse (>100km). On the other hand, nadir sounders measure brightness temperature (TB) that can be related to the temperature and water vapor structure in the atmospheric column with higher horizontal resolution (∼25 km). However, retrievals from passive sounders have lower vertical resolution (>2km), and are complicated by precipitation, clouds, and surface emissivity uncertainty over land.

In this study we combine these two complementary types of observations by use of a novel tomography method to improve the 3D characterization of water vapor in the LT. This is done by adjusting the water vapor density along the RO links to match the RO observations, while preserving the horizontal water vapor variability based on information derived from the nadir sounders. We test this method using simulations based on mesoscale model outputs from the Weather Research and Forecasting Model (WRF), as well as real observations from RO and Cross-track Infrared Microwave Sounder Suite (CrIMSS). We demonstrate that the tomographic retrieval can resolve the complex moisture structure better than what is possible from either measurement alone.

1 Introduction

The lower troposphere (LT) between 0-6 km altitude plays an essential role in radiative transfer, land surface-atmosphere feedback, convective initiation, and water and energy cycles (Stevens et al., 2017; Sherwood et al., 2010; Mülmenstädt et al., 2021; Zhou et al., 2016). Predictability of extreme weather/climate events and future water/energy budgeting largely relies

https://doi.org/10.5194/egusphere-2026-4427
Preprint. Discussion started: 11 August 2026

on the knowledge of these complicated and non-linearly connected processes in the LT (Fujita and Sato, 2017; Holloway and Neelin, 2009). To better understand the cause, impact, and interaction of these processes, it is critical to have accurate representation of the three-dimensional temperature and water vapor fields in the LT (Wulfmeyer et al., 2015). Depending on the application, the required resolution in observing the LT may vary; however, in most cases, including weather and climate monitoring, forecast verification, and data assimilation applications, 300m vertical and 20km horizontal resolutions (meso-beta) are needed (Wulfmeyer et al., 2015). Currently, no single spaceborne thermodynamic observation technique can reach both of these vertical and horizontal resolutions. The most impactful observations in numerical weather prediction (NWP) come from passive microwave radiometers (MWR), which utilize radiances across multiple frequency bands to retrieve the vertical structure of temperature and water vapor in the atmospheric column (Rodgers, 2000). While MWR's footprint retains 20km horizontal resolution, the vertical resolution of 2km is strictly limited by its nature as a nadir sounder. The same limitation applies to other nadir sounding techniques: observations from hyperspectral infrared sounders (IR) can reach less than 20km horizontal resolution while the vertical resolution is 1km; Near-IR (NIR) imagers provide the best spaceborne horizontal resolution (1-2km), but can only retrieve vertically integrated water vapor. Differential absorption lidar (DIAL) and temperature rotational Raman LIDAR (TRRL) offer vertical resolutions of ∼300m and horizontal resolution of ∼100m. However, the high power consumption and antenna requirements of these instruments restrict their applications to suborbital flights, thereby limiting their impacts on NWP (Teixeira et al., 2021). By contrast, the Global Navigation Satellite System – Radio Occultation (GNSS-RO) provides great vertical resolution (200m) but poor horizontal resolution (100-200km) (Kursinski et al., 1997). The complementary strengths of spaceborne nadir sounders and RO limb measurements in resolving different dimensions motivate this study to integrate both techniques in order to obtain the 3D LT thermodynamic field with an optimal resolution.

While the presented method can be applied to most spaceborne limb and nadir sounding techniques, in this article we focus on GNSS-RO and MWR to illustrate its applicability. As a limb sounding technology, GNSS-RO measures the received excess phase delay induced by the atmosphere and computes the bending angle of each ray path due to refraction through the atmosphere. The GNSS L-band frequencies (approximately 1.1–1.6 GHz) allows the RO signal to penetrate through heavy cloud cover and precipitation which are abundant in the LT. The computed bending angle can then be inverted to retrieve the vertical refractivity profiles, and by use of auxiliary information, the vertical thermodynamic profiles can be accurately observed. Since the launch of GPS/MET in 1995, the number of RO missions has steadily increased and now includes several commercially operated satellites. Today, RO observations exceed 10,000 per day, offering a dense and global coverage. With radio holographic processing of GNSS-RO, vertical resolution can reach 100m in the LT. However, the long ray path in the direction of the link leads to a low horizontal resolution of 100-200km. Conversely, MWR observes across multiple frequency bands in nadir-viewing geometry to provide information related to the vertical structure of temperature and water vapor in the atmospheric column. Traditionally, the thermodynamic profiles are retrieved along with the surface temperature and emissivity simultaneously through an optimal estimation approach (Boukabara et al., 2011). MWR observations have been utilized extensively and it has been shown to have significant positive impacts in NWP with assimilation of observations from AMSU/MHS (Bao et al., 2015), AMSR-E (Kazumori et al., 2008), and ATMS (Bormann et al., 2013). But MWR sounding also suffers from poor vertical resolution (>2km) due to weighting functions with a relatively wide vertical extent. MWR measurements

https://doi.org/10.5194/egusphere-2026-4427
Preprint. Discussion started: 11 August 2026

and retrievals from different frequency bands also contain forward modeling uncertainties caused by clouds, precipitation, absorption, and surface properties.

The idea of combining the nadir and limb soundings has been proposed numerous times in the past. Borbas et al. (2003) and Ho et al. (2007) developed the multivariable regression method to estimate the 1D atmospheric thermodynamic states based on coefficients trained by a set of collocated RO refractivity and MWR/IR brightness temperature observations. Collard and Healy (2003) also showed that the complementary RO and nadir sounding (MWR/IR) measurements can be fused together by using a sequential 1DVar algorithm to significantly increase the impacts of the observations in NWP models. Nevertheless, GNSS-RO refractivity observation itself could be negatively biased in the LT for several reasons including ducting (Ao, 2007), low SNR (Wang et al., 2016), and small-scale refractivity fluctuations (Gorbunov et al., 2015). In particular, the refractivity computed from the unbiased bending angle will be negatively biased through the conventional retrieval process under ducting conditions (Xie et al., 2006; Ao, 2007). This translates into a positive bias in temperature and a negative bias in water vapor within the boundary layer. To reduce the negative refractivity bias due to ducting, Wang et al. (2017) reconstructed the observed profile based on an optimal estimation approach which combined RO and AMSR-E total precipitable water (TPW) retrievals. Wang et al. (2024) extended this study further by combining RO bending angle with MWR brightness temperature measurements using 1DVar to retrieve the LT thermodynamic profiles. However, thus far, most of the proposed methodology focuses on 1D combination of collocated observations and don't account for the true footprint of nadir sounders or GNSS-RO elongated ray path to construct a 3D thermodynamic field. Although a tomographic approach has been applied to RO measurements in the Mars atmospheric environment (Moeller et al., 2021), the combination of nadir and limb sounding to construct a 3D field has not been explored on Earth or Mars.

In this study, a 3D-tomography approach is developed and implemented to preserve the high vertical resolution from GNSS-RO and high horizontal resolution from MWR for the LT thermodynamics characterization. While the methodology assumes unbiased RO refractivity retrievals, in practice, it can be applied after the observed profiles have been reconstructed according to the method described in Wang et al. (2017). The tomographic algorithm is introduced in detail in Sec. 2. Results from simulations and actual data from collocated GNSS-RO and ATMS measurements are presented and discussed in Sec. 3. A conclusion is given in Sec. 4.

2 Methodology

We divide the 3D space to be imaged into grids along fixed longitudes, latitudes, and altitudes. Fig. 1 shows this 3D grid flattened into a Euclidean geometry. The curved lines represent the RO links which are approximately straight lines in spherical coordinates but appear curved in this Euclidean geometry. Each voxel is associated with a grid coordinate defined by its latitude (ϕ), longitude (θ), and height (z). We take the size of each voxel to be $0.1^\circ \times 0.1^\circ$ in the horizontal direction to capture the horizontal resolution of MWR footprint and 200 m in the vertical direction to match the vertical resolution of GNSS-RO. The temperature T, water vapor e, and refractivity N are modeled as piecewise constant within each voxel and are denoted

https://doi.org/10.5194/egusphere-2026-4427
Preprint. Discussion started: 11 August 2026

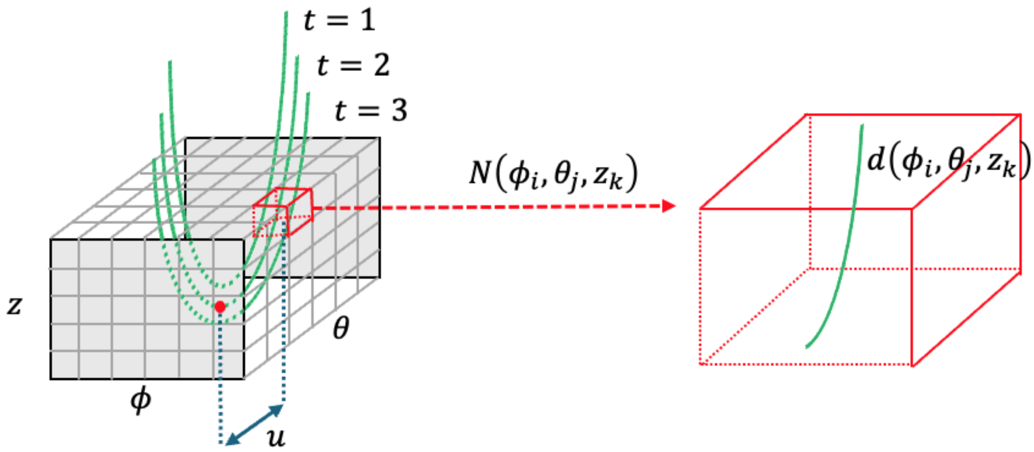

Figure 1. The voxel coordinate system defined throughout this study, and a representation of the RO links (green lines). The red dot shows the tangent point location of one of the ray paths. The voxel highlighted by red lines along with the ray path going through it are magnified on the right.

as $T(\phi_i,\theta_j,z_k)$, $e(\phi_i,\theta_j,z_k)$, and $N(\phi_i,\theta_j,z_k)$ where i, j, and k are the indices in latitude, longitude, and height grids, respectively.

We estimate the 3D refractivity field $N(\phi_i,\theta_j,z_k)$ by combining temperature T_{nadir} and water vapor e_{nadir} profiles derived from the MWR retrievals at each footprint and GNSS-RO 1D refractivity retrieval. Unlike conventional variational methods, the background in this approach is the refractivity derived directly from MWR retrieved profiles rather than from a numerical model or analysis data, thereby minimizing the model-induced errors (except through the dependence of the MWR retrievals on the model). Since the 1D GNSS-RO refractivity profiles provide essential vertical information while the nadir sounders give horizontal information, we assume the true refractivity field $N(\phi_i,\theta_j,z_k)$ to be linearly related to the nadir refractivity $N_{nadir}(\phi_i,\theta_j,z_k)$ (derived from the nadir retrieved temperature and water vapor) at each level as follows:

$$N(\phi_i,\theta_j,z_k) = N_{nadir}(\phi_i,\theta_j,z_k)\cdot a(z_k) \tag{1}$$

where $a(z)$ is a scale factor for each layer to be determined by use of GNSS-RO observations. The main point of this scaling, introduced in (Hajj et al., 1994) in the context of ionospheric profiling using ionospheric RO data, can be described as follows. The starting point of the tomography inversion process is $N_{nadir}(\phi_i,\theta_j,z_k)$ which, due to the geometry of the nadir sounders, has high horizontal and low vertical resolutions. The scaling in Eq. (1) allows one to maintain the horizontal resolution of $N_{nadir}(\phi_i,\theta_j,z_k)$ while refining its vertical resolution by introducing a high resolution scaling factor $a(z_k)$ at each layer. Stated differently, N_{nadir} for a given voxel is strongly correlated with neighboring voxels in the same vertical column. The scaling factor $a(z)$, solved for by use of GNSS-RO data, allows for breaking down this correlation. To combine the temperature and water vapor derived from the nadir sounders with GNSS RO observations, forward operators for both types of instruments are needed and are described below.

https://doi.org/10.5194/egusphere-2026-4427
Preprint. Discussion started: 11 August 2026

2.1 The Forward Operators

2.1.1 Microwave Radiometer

The nadir instrument retrievals (temperature and water vapor), used as a priori in the retrieval process, are linearly interpolated to the voxel grid defined above (see Fig. 1). The refractivity of each voxel $N_{nadir}(\phi_i,\theta_j,z_k)$ can be calculated using the following equation (Smith and Weintraub, 1953):

$$N_{nadir}(\phi_i,\theta_j,z_k) = 77.6\frac{p_{nadir}(\phi_i,\theta_j,z_k)}{T_{nadir}(\phi_i,\theta_j,z_k)} + 3.73\times10^5\frac{e_{nadir}(\phi_i,\theta_j,z_k)}{T^2_{nadir}(\phi_i,\theta_j,z_k)} \tag{2}$$

where T_{nadir}, p_{nadir}, and e_{nadir} are temperature, total pressure, and water vapor partial pressure respectively from the nadir instrument retrieval. The calculated refractivity is used as the a priori for the following tomographic processing. For simulation purposes, the simulated "true" temperature and water vapor fields were linearly smoothed (2 km vertically and 10 km horizontally) before interpolation to match the MWR observation footprint. For real observations, the nadir retrievals from the Cross-track Infrared Microwave Sounder Suite (CrIMSS) dataset (Smith, 2019) were used and interpolated to the voxel grid without additional smoothing.

2.1.2 GNSS-RO

The commonly used RO total excess phase observable,

$$\Phi = \int n dl_c - \int dl_s \tag{3}$$

is the difference between the optical path length of the refracted ray and the straight-line geometric path in vacuum, represented by the red and black lines connecting the GNSS and LEO satellites in Fig. 2, respectively. Through the process of careful calibration of clocks and orbits, this total excess phase observable can be measured throughout an RO, up to an unknown constant (Hajj et al., 2002). To appreciate the distinct geometric and optical contributions to this total excess phase observable, we decompose the index of refraction as $n = 1 + N\times10^{-6}$. Eq. 3 can then be written as

$$\Phi = (L_c - L_s) + 10^{-6}\int N dl_c \tag{4}$$

where L_c and L_s are the geometric lengths of the curved and straight paths, respectively. Therefore, the total excess phase contains a purely geometric term due to ray bending (i.e., the $L_c - L_s$ term in Eq. (4)) and a refractivity-dependent term due to the atmosphere (the second term on the RHS of Eq. (4)). To isolate the atmospheric contribution, we define the partial excess phase as:

$$\Phi_p = [\Phi - (L_c - L_s)]\times10^6 = \int N(\phi_i,\theta_j,z_k)\,dl_c. \tag{5}$$

Unlike the total excess phase defined in Eq. 3, this partial excess phase depends only on the refractivity along the portion of the ray path within the atmosphere where $N > 0$, eliminating contributions from vacuum regions. As a result, forward

https://doi.org/10.5194/egusphere-2026-4427
Preprint. Discussion started: 11 August 2026

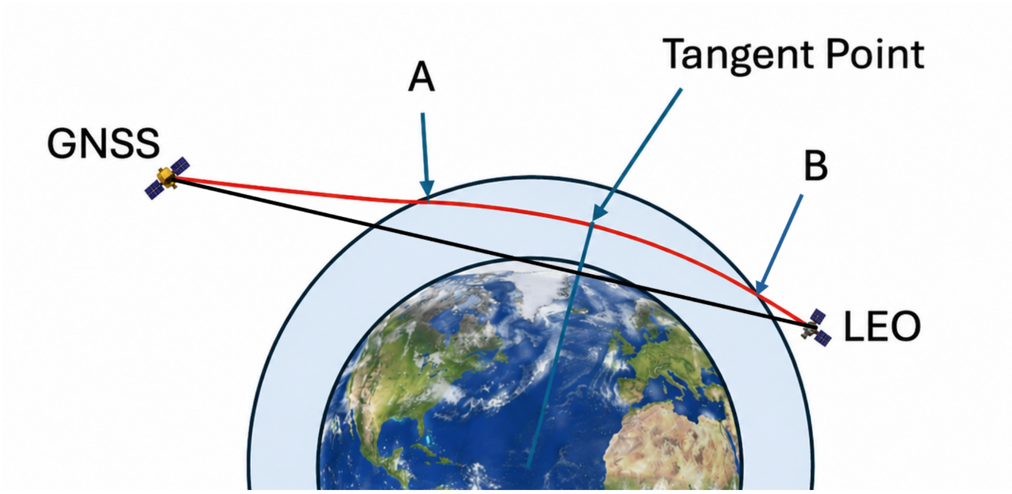

Figure 2. Radio occultation geometry illustration showing the difference between total excess phase and partial excess phase.

modeling can be restricted to the atmospheric domain without requiring integration along the full ray path. This simplifies the tomographic inversion significantly and can be applied when doing simulations and in the processing of real observations.

In simulation mode, the simulated partial excess phase Φ_p is generated by integrating through the three-dimensional refractivity field $N(\phi_i, \theta_j, z_k)$ (taken as truth) along the curved ray path l_c within the modeled domain:

$$\Phi_p = \int_A^B N(\phi_i, \theta_j, z_k)\, dl_c. \tag{6}$$

where points A and B correspond to the intersection of the ray with the upper boundary of the atmosphere (see Fig. 2). This is done by starting at height z_k as the tangent point and then trace the ray path on both sides of the tangent point through the refractivity field. The ray is propagated outward until it intersects points A and B, corresponding to the upper boundary of the modeled region on each side. In this way, the integral is restricted to the simulated domain, eliminating the need to model the ray paths all the way to the satellites.

When processing real GNSS-RO observations, the true three-dimensional refractivity is not available. What is available is a one-dimensional vertical refractivity profile $N_{RO}(z)$, obtained via bending angle inversion using the Abel transform under the assumption of spherical symmetry. This assumption implies that refractivity depends only on height, where $N(\phi, \theta, z) \approx N_{RO}(z)$, so that horizontal variations are neglected and each atmospheric layer is treated as spherically uniform. However, because the retrieved profile $N_{RO}(z)$ reproduces the same observed phase delay under this spherical symmetry assumption, the forward model remains consistent if the true refractivity field is replaced by $N_{RO}(z)$. In other words, the error introduced into $N_{RO}(z)$ due to the spherical symmetry assumption, cancels out when doing the forward raytracing using $N_{RO}(z)$ instead of $N(\phi, \theta, z)$ to derive the partial excess phase (Syndergaard et al., 2005). Accordingly, the partial excess phase can be expressed

https://doi.org/10.5194/egusphere-2026-4427
Preprint. Discussion started: 11 August 2026

as

$$\Phi_p = \int_A^B N_{RO}(z_k)\, dl_c. \tag{7}$$

As in the case of simulated data, when processing real observations, raytracing starts at a tangent point (as determined by the Abel inversion) and is done on both sides of the tangent point until the rays intersect the upper bound of the imaged domain with intersection corresponding to points A and B of the integral in Eq. (7).

Eqs. (6) and (7) are evaluated using two-dimensional ray tracing in the occultation plane, following the same methodology implemented in the Radio Occultation Processing Package (ROPP) (ROPP document, 2020) (Culverwell et al., 2015). The details of the implementation are given in Appendix A. For a given set of tangent point locations, only knowledge of the occultation plane is needed at any given time such that the raytracing is done in that plane. The exact positions of the GNSS transmitter or receiver are not needed. This is true when processing simulated or real data. We sample the ray path within the 3D domain with the incremental segment of $\Delta s = 20m$, which is sufficiently small relative to the grid size used in the inversion. By locating the latitude, longitude, and height of each point along the ray path with the voxel grid defined at the beginning of this section, the number of points for each voxel can be counted. Therefore, the path length within each voxel $d(\phi_i, \theta_j, z_k)$ as shown in Fig. 1 can be estimated:

$$d(\phi_i, \theta_j, z_k) = M(\phi_i, \theta_j, z_k) \times \Delta s \tag{8}$$

where $M(\phi_i, \theta_j, z_k)$ is the number of ray path sample points at each voxel. Having determined the ray path length in each voxel, the partial excess phase for each ray path given in Eq. (6) can be discretized as:

$$\Phi_p = \sum_{l_c} N(\phi_i, \theta_j, z_k) \cdot d(\phi_i, \theta_j, z_k) \tag{9}$$

Only those voxels where ray path l_c penetrates through will contribute to the partial excess phase, since $d(\phi_i, \theta_j, z_k) = 0$ at the other voxels even though their refractivity is non-zero valued. As a discretized version of Eq. 6, this equation will be used in simulation to generate the GNSS-RO observable for tomography. For real GNSS-RO data, the following discretized equation corresponding to Eq. 6 will be used:

$$\Phi_p = \sum_{l_c} N_{RO}(z) \cdot d(\phi_i, \theta_j, z_k) \tag{10}$$

2.2 Level-wise 3D Tomography

The goal of the proposed tomography approach is to estimate the true 3D field solution that best matches the partial excess phase Φ_p observations based on the given a priori field $N_{nadir}(\phi_i, \theta_j, z_k)$ obtained from the nadir retrievals. Due to the nature of nadir and limb viewing geometry, we assume that the horizontal information of the estimated solution come mainly from the nadir observations, while GNSS-RO provides finer resolution in the vertical direction. As shown in Eq. 1, the ratio of refractivity between each voxel in the same layer z_k is constrained by the a priori so that only the estimation of the vertical

https://doi.org/10.5194/egusphere-2026-4427
Preprint. Discussion started: 11 August 2026

scaling factor $a(z)$ is needed instead of the entire refractivity set of $N(\phi_i, \theta_j, z_k)$ in that layer. This approach simplifies the computational complexity significantly by reducing the number of state variables from the total number of voxels in 3D space to the number of vertical layers, i.e., collapsing a 3D problem into a 1D problem. Using the constraint defined in Eq. 1, our model equation can be written as

$$\Phi_p = \sum_{l_c} N_{nadir}(\phi_i, \theta_j, z_k) \cdot d(\phi_i, \theta_j, z_k) \cdot a(z) \tag{11}$$

where $a(z)$ are the parameters to be solved for and are given by

$$\hat{a}(z) = \left[\sum_{l_c} N_{nadir}(\phi_i, \theta_j, z_k) \cdot d(\phi_i, \theta_j, z_k) \right]^{\dagger} \cdot \Phi_p \tag{12}$$

where † is the pseudo inverse operator [see, e.g., Hajj et al. (1994)].

After obtaining the estimated vertical scaling factor $\hat{a}(z)$ and using Eq. 1 again, we can now estimate the refractivity field solution at each grid as

$$\hat{N}_{sol}(\phi_i, \theta_j, z_k) = N_{nadir}(\phi_i, \theta_j, z_k) \cdot \hat{a}(z) \tag{13}$$

By assuming the temperature and pressure fields from the nadir instrument retrieval to be sufficiently accurate, one can use Eq. 2 to calculate vapor pressure from the estimated 3D refractivity field. In our approach, we also assume the change of the ray path due to refractivity difference between the estimated field and the a priori to be negligible, and that the same ray tracing solution can be applied to all subsequent iterations. The assumption is mostly valid because the ray path difference due to refractivity is normally less than $1m$ per voxel.

While the derived weighting factor $\hat{a}(z)$ can be applied to the entire refractivity field at a given layer, we limit its application to the voxels within 2° (200km) horizontal distance from the tangent point location. This is due to the fact that the total length of GNSS-RO ray paths within the domain does not exceed 3°, which limits the horizontal sensitivity of the RO observations to scales of that order. We define u as the horizontal distance between a voxel and the tangent point location, as illustrated in Fig. 1. Within the 2° horizontal range, a Hann window weighting function $H(u)$ is applied to taper the GNSS-RO contribution such that the solution transitions smoothly from the RO-constrained retrieval near the tangent point to the a priori field farther away. The Hann window is given by

$$H(u) = \begin{cases} \frac{1}{2}\left[1 + \cos\left(\pi \frac{u}{u_{\max}}\right)\right], & 0 \le u \le u_{\max}, \qquad u_{\max} = 2^\circ, \\ 0, & \text{otherwise.} \end{cases} \tag{14}$$

The resulting normalized refractivity at each voxel within the 2° of a single tangent point can then be written as:

$$\hat{N}(\phi_i, \theta_j, z_k) = \hat{N}_{sol}(\phi_i, \theta_j, z_k) \cdot H(u) + N_{nadir}(\phi_i, \theta_j, z_k) \cdot [1 - H(u)] \tag{15}$$

https://doi.org/10.5194/egusphere-2026-4427
Preprint. Discussion started: 11 August 2026

The purpose of Eq.15 is to construct a smooth spatial transition between the refractivity solution constrained by a GNSS radio occultation (RO) observation and the background refractivity field derived from the nadir retrieval. The same logic can be extended to the case where a voxel lies within the influence region of two separate RO observations. In this case, each occultation contributes according to its corresponding distance from the voxel. Let u_1 and u_2 denote the distances to the two tangent points, and let $\hat{N}_{sol,1}$ and $\hat{N}_{sol,2}$ denote the refractivity solutions associated with each occultation. A combined RO solution can then be constructed as a normalized weighted average:

$$\hat{N}_{sol,T} = \frac{\hat{N}_{sol,1}H(u_1) + \hat{N}_{sol,2}H(u_2)}{H(u_1) + H(u_2)}. \tag{16}$$

This expression ensures that the RO solution closer to the voxel contributes more strongly, while preserving smooth continuity between overlapping RO influence regions. The normalization by $H(u_1) + H(u_2)$ guarantees that the combined RO contribution remains properly scaled. The transition between the combined RO solution and the nadir retrieval is then determined by the residual weighting not accounted for by either RO observation. Since $1 - H(u)$ represents the lack of constraint from a given RO profile, the residual weight assigned to the nadir retrieval for two occultations is expressed as

$$(1 - H(u_1))(1 - H(u_2)). \tag{17}$$

The final refractivity field can therefore be written as

$$\hat{N} = \hat{N}_{sol,T}\left[1 - (1 - H(u_1))(1 - H(u_2))\right] + N_{nadir}(1 - H(u_1))(1 - H(u_2)). \tag{18}$$

Expanding the complement term yields

$$1 - (1 - H(u_1))(1 - H(u_2)) = H(u_1) + H(u_2) - H(u_1)H(u_2), \tag{19}$$

which shows that the total RO contribution behaves similarly to an inclusion–exclusion formulation: the individual RO contributions are added while the overlap term prevents double counting in regions where both occultations contribute simultaneously.

This framework naturally generalizes to an arbitrary number M of RO observations. For M occultations with corresponding distances u_m and RO-derived solutions $\hat{N}_{sol,m}$, the combined RO solution may be expressed as

$$\hat{N}_{sol,T} = \frac{\sum_{m=1}^{M} \hat{N}_{sol,m} H(u_m)}{\sum_{m=1}^{M} H(u_m)}. \tag{20}$$

The residual nadir weighting becomes

https://doi.org/10.5194/egusphere-2026-4427
Preprint. Discussion started: 11 August 2026

$$\prod_{m=1}^{M}\left[1-H(u_m)\right], \tag{21}$$

which represents the fraction of the voxel not constrained by any RO observation. The final blended refractivity field is therefore

$$\hat{N}=\hat{N}_{sol,T}\left[1-\prod_{m=1}^{M}(1-H(u_m))\right]+N_{nadir}\prod_{m=1}^{M}(1-H(u_m)). \tag{22}$$

This formulation provides a smooth and physically consistent transition between localized RO constraints and the large-scale nadir retrieval while naturally accommodating overlapping sensitivity regions from multiple occultations.

3 Results

3.1 WRF simulation

To evaluate the feasibility and efficacy of this tomography algorithm, we apply it to the Weather Research and Forecast (WRF) mesoscale simulation output. Here a WRF case of a strong Pacific cold front on 2006-12-15:00 UTC with a complex 3D thermodynamic structure is chosen as an example. The domain of the simulation is within 30 to 36° latitude ($\sim$ 0.005° resolution) and -150 to -140° in longitude ($\sim$ 0.04° resolution). The WRF domain is linearly interpolated to the 3D grid defined in the previous section.

To illustrate the 2D ray tracing we propagate the ray using Eqs. A1-A4 on a single vertical plane which has constant latitude (33°). The ray paths are shown as cyan curves in Fig. 3. As the color in the background suggests, the moist air extends from the surface up to $\sim$4km throughout the domain, and the dry air intrusion occurs between -150 to -143° longitude, separating the moist air into a lower branch within 2km and an upper tongue between 3-4 km. This case is chosen intentionally for its complicated vertical structure to illustrate the capability of limb/nadir sounding tomography, and will be used for our simulations described in the following subsections.

3.1.1 Single occultation plane

We first demonstrate the water vapor characterization improvement using the proposed tomography algorithm on a single vertical occultation plane (latitude = 33°). In this case we randomly choose our tangent point location at -143.17° longitude, with height interval of 0.12km between each ray path within the range of 0-8km. All the ray paths propagate along the same vertical plane at 33° latitude and the height interval is selected based on the GNSS-RO vertical resolution. The GNSS-RO partial excess phase observation for each ray path is simulated by Eq. 9 along the propagated ray path within the defined 2D refractivity field $N(\phi_i,\theta_j,z_k)$ in the occultation plane. As discussed in the previous section, the GNSS-RO partial excess phase observation can be calculated from the segment of the ray path located within the domain, and therefore extending the

https://doi.org/10.5194/egusphere-2026-4427
Preprint. Discussion started: 11 August 2026

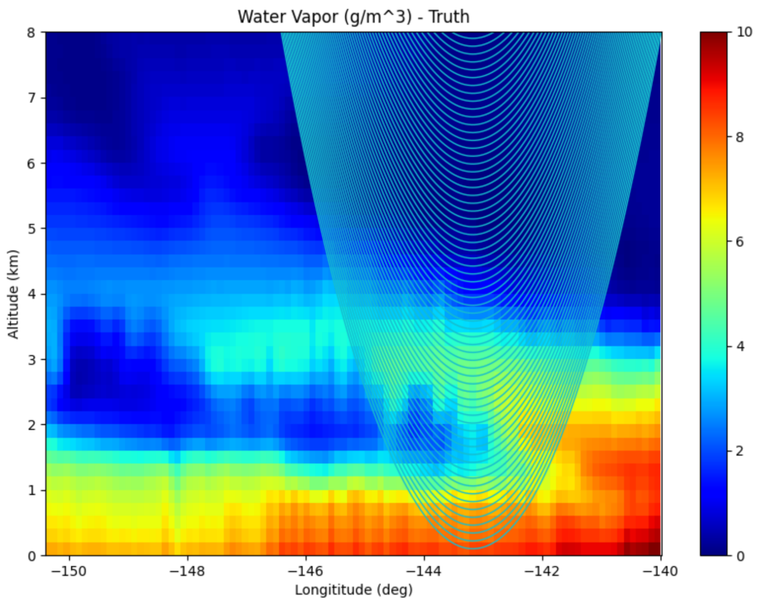

Figure 3. The propagated ray path (shown in cyan color) using 2D ray tracing on a single vertical plane of the WRF model. The background color represents the water vapor quantity at each grid.

refractivity beyond the domain is not needed. These simulated observations are then applied to the tomography algorithm and combined with the corresponding a priori computed by smoothing the true field from WRF as stated in Sec. 2.1.1. Here a boxcar smoothing with 2km vertical window and 0.2° is applied. The resulting refractivity field can then be used to derive the water vapor solution by using Eq. 2 and assuming the temperature a priori to be true. The results are shown in Fig. 4

The upper-left panel in Fig. 4 is the water vapor content of WRF model along the occultation plane, which serves as the true field in this study. The upper-right panel is the linearly smoothed domain on the same plane that simulates the MWR retrieval and is used as a priori. It can be seen that the intrusion structure has become much less defined because of poor vertical resolution after smoothing. The water vapor solution obtained by combining the a priori with a single RO measurement using the tomography approach introduced in the previous section is shown in the lower-left panel. In this panel a localized "hole" in water vapor appears near 2km between -142 and -144° longitudes relative to the a priori result, bringing the retrieval into closer agreement with the truth field in that region. This occurs because the ray paths passing through the moisture-gap voxels experience smaller partial excess phase delays than predicted by the a priori field. The tomography inversion interprets these reduced delays as evidence of lower refractivity within those voxels, resulting in retrieved weighting values $a(z)$ smaller than unity and consequently a reduction in the retrieved water vapor in that region. Furthermore, since the weights $a(z)$ are applicable only within ±2deg w.r.t. the tangent point location due to the Hann window, the range of the hole is limited to the area close to the tangent points. Note that in this panel only the lowest ray path is shown to indicate the location of the RO tangent point but the results are obtained using all the ray paths as shown in Fig. 3.

https://doi.org/10.5194/egusphere-2026-4427
Preprint. Discussion started: 11 August 2026

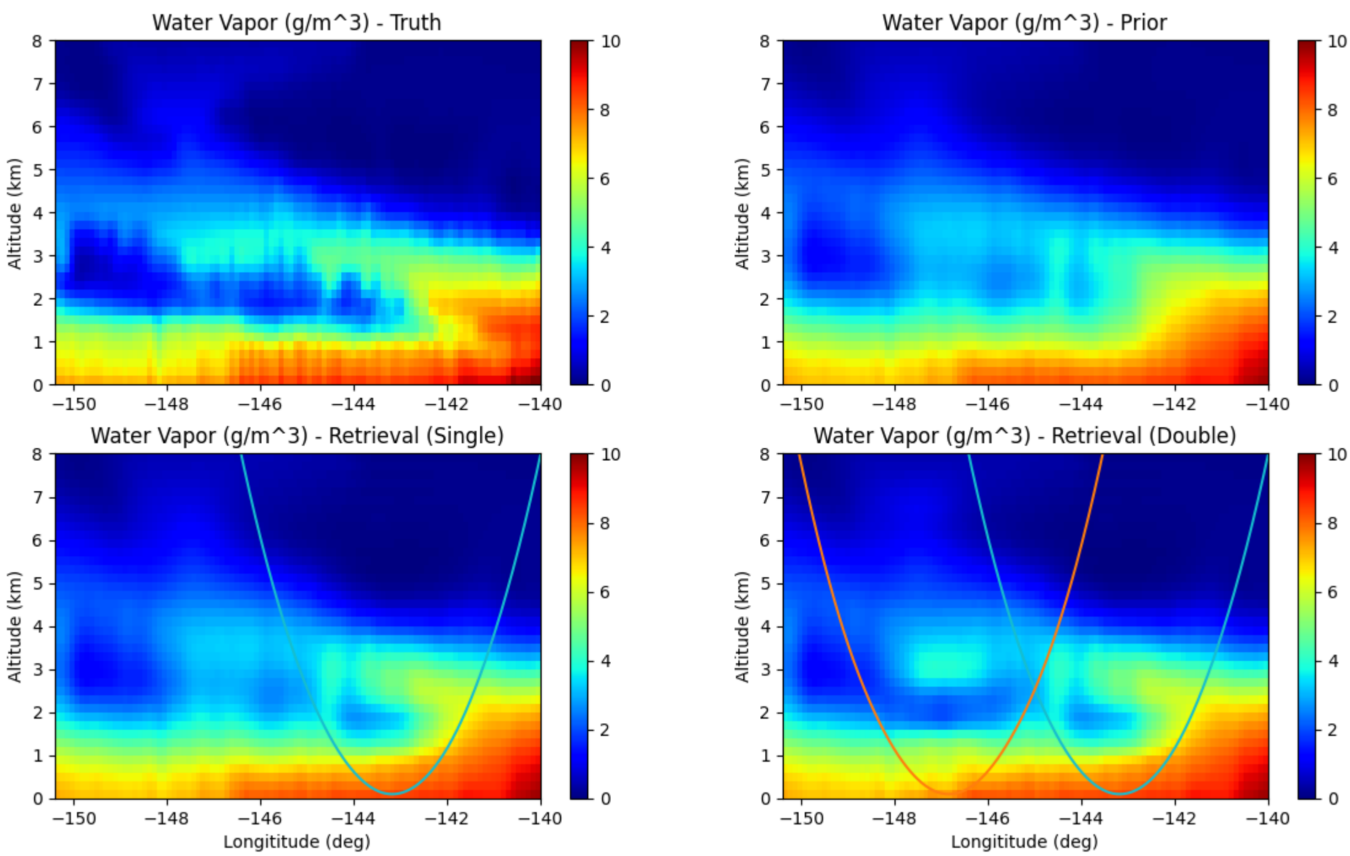

Figure 4. Upper-left: The WRF model in the occultation plane used as truth domain. Upper-right: Smoothed WRF domain representing the MWR retrieval and used as a priori in the tomography algorithm. Lower-left: Results of the tomography algorithm with a single RO. Only the lowest ray of the RO is shown. Lower-right: Same as lower-left panel but with 2 ROs. The lowest link for the second RO is shown on the left in orange.

A second RO at the -146.83° longitude (orange dotted line) in the same occultation plane is added to the first RO with the resulting retrieval shown in the lower-right panel of Fig. 4. In this case, a vapor gap appears between -145 and -149° longitudes and 2-3km heights separating the vapor located above and below, with an increase of water vapor value at ∼3 km. Statistically, the water vapor RMSE over the occultation plane is reduced by 22% from 0.477 g/m^3 of nadir sounding only, to 0.37 g/m^3 with two GNSS-RO added. The result better matches the cold front intrusion structure shown in the true vapor profile (upper left panel) and significantly improves the simulated nadir-only retrieval.

Because of the Hann window defined in Eq. 14 and used in Eqs. 15 and 22, the tomographic solution at each column will depend on its distance to each GNSS-RO tangent point. The further away the column is from the tangent point, the closer the solution will be to the nadir retrieval. This behavior is illustrated in Fig. 5, which shows six vertical water vapor profiles at

https://doi.org/10.5194/egusphere-2026-4427
Preprint. Discussion started: 11 August 2026

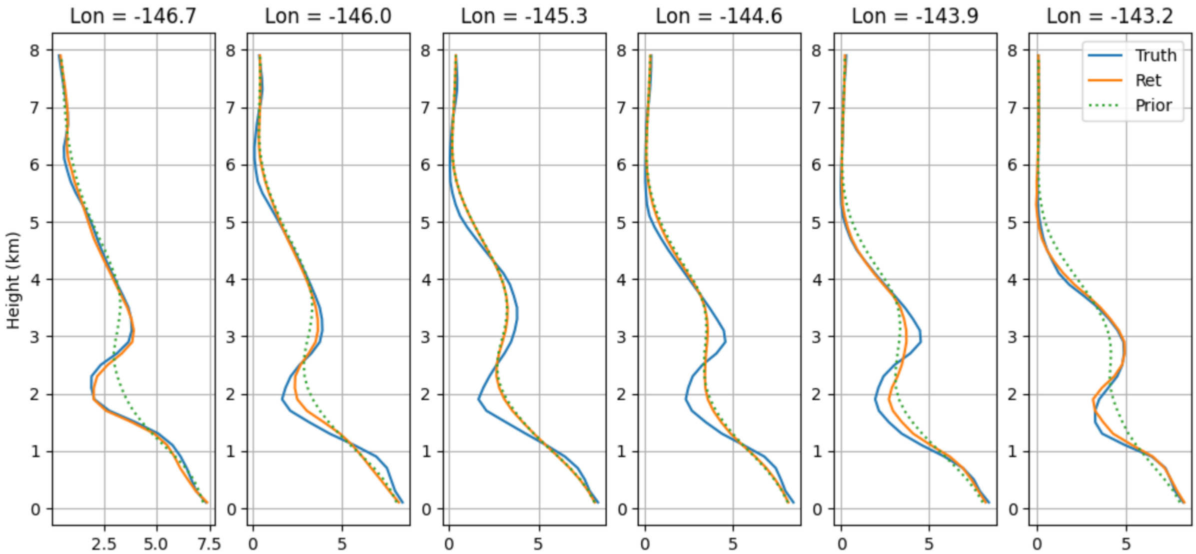

Figure 5. Six vertical water vapor profiles along the occultation plane between the two tangent points (Lon = -146.7 and Lon = -143.2) shown in Fig. 4. The true profiles are shown in blue, the tomography solutions are shown in orange, and the a priori (nadir retrieval) are shown in dotted green. The tomography solutions align with the true profiles in regions close to the RO tangent points at both ends and revert back to the a priori away from the tangent points.

different longitudes along the occultation plane (latitude $= 33°$) presented in Fig. 4. The profiles extend from the tangent point location of the orange occultation on the left to that of the cyan occultation on the right.

In the first panel from the left in Fig. 5, the tomography solution (orange line) closely matches the true profile (blue line), indicating that the weighting derived from the nearby GNSS-RO observation correctly captures the vertical structure. However, as the profile location moves farther away from the tangent point (e.g., at longitudes $-145.3°$ and $-144.6°$), the tomography solution gradually deviates from the truth profile and overlaps with the nadir retrieval (green dashed line). This indicates that the voxels at those locations are too far from the GNSS-RO tangent point for the retrieved vertical weighting to have an effect. As a result, the solution smoothly reverts back toward the nadir retrieval, consistent with the horizontal tapering imposed by the Hann window weighting. Closer to the second tangent point on the right (longitudes $-143.9°$ and $-143.2°$), the tomography solution once again approaches the true profile as the influence of the second GNSS-RO observation increases.

In the above example, even though the tomography has been applied on the occultation plane, the improvement can also be observed in the voxels out of the occultation plane. This is demonstrated in Fig. 6 which shows a horizontal cross section of the 3D domain at 2km height. Comparing the a priori (upper-right) with the truth (upper-left) in Fig. 6 one can observe that the horizontal water vapor structure of the a priori is generally smoother than the truth, reflecting the smoothing effect of the MWR retrievals. At some locations such as -150 to -140° longitude and 32° latitude it is positively biased due to the contribution from the voxels below 2km. By combining the biased a priori with a single RO observation (with a ray path trajectory shown as the orange solid line at 33° north latitude between -142° and -144° longitudes of the lower-left panel), the water vapor drops

https://doi.org/10.5194/egusphere-2026-4427
Preprint. Discussion started: 11 August 2026

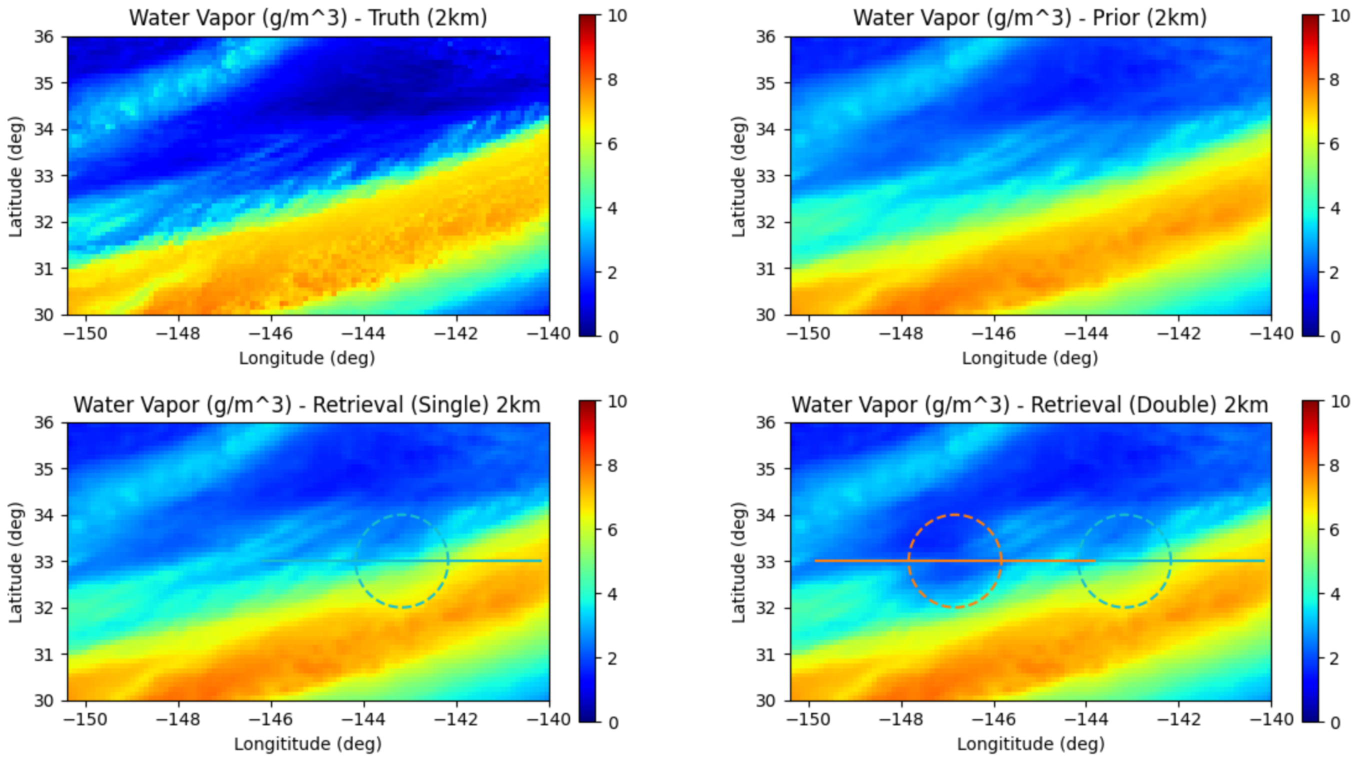

Figure 6. Same area as Fig. 4 but for a horizontal cross section of the 3D field at altitude = 2km. The solid line represents the RO plane. Each dashed circle in the lower panels is centered at the RO tangent point and represents the circle of influence introduced by the weights $a(z)$ and the Hann window.

by ∼0.5 g/m3 within a circle of 1° radius centered at the tangent point indicated by the cyan dashed circle. The drop is more obvious when we add an additional RO as shown in the lower-right panel: the water vapor within the orange dashed circle dropped substantially and agrees better with the truth field.

3.1.2 Multiple occultations in 3D

In general, ROs do not align in one plane in the way they were analyzed thus far. In this section, we apply a more realistic RO coverage in 3D with a distribution obtained from a hypothetical constellation of 12 LEO satellites in different orbits tracking all global GNSS constellations (GPS, Galileo, GLONASS, BeiDou) that does not limited to the single occultation plane condition. Under this scenario, 34 occultations were collected during a 12-hr period within the 3D domain we have been examining. We apply the tomographic algorithm introduced in Sec. 2 in three different scenarios where 5, 10 and 20 randomly chosen ROs are combined with the same a priori as before and compared to the truth given by the WRF model.

The 3D tomography results are shown in Figs. 7 that showing the 33° latitude vertical cross section, and 8 that showing a 2km altitude horizontal cross section. The cyan solid lines at each panels in Fig. 7 are ray path trajectory at the lowest tangent

https://doi.org/10.5194/egusphere-2026-4427
Preprint. Discussion started: 11 August 2026

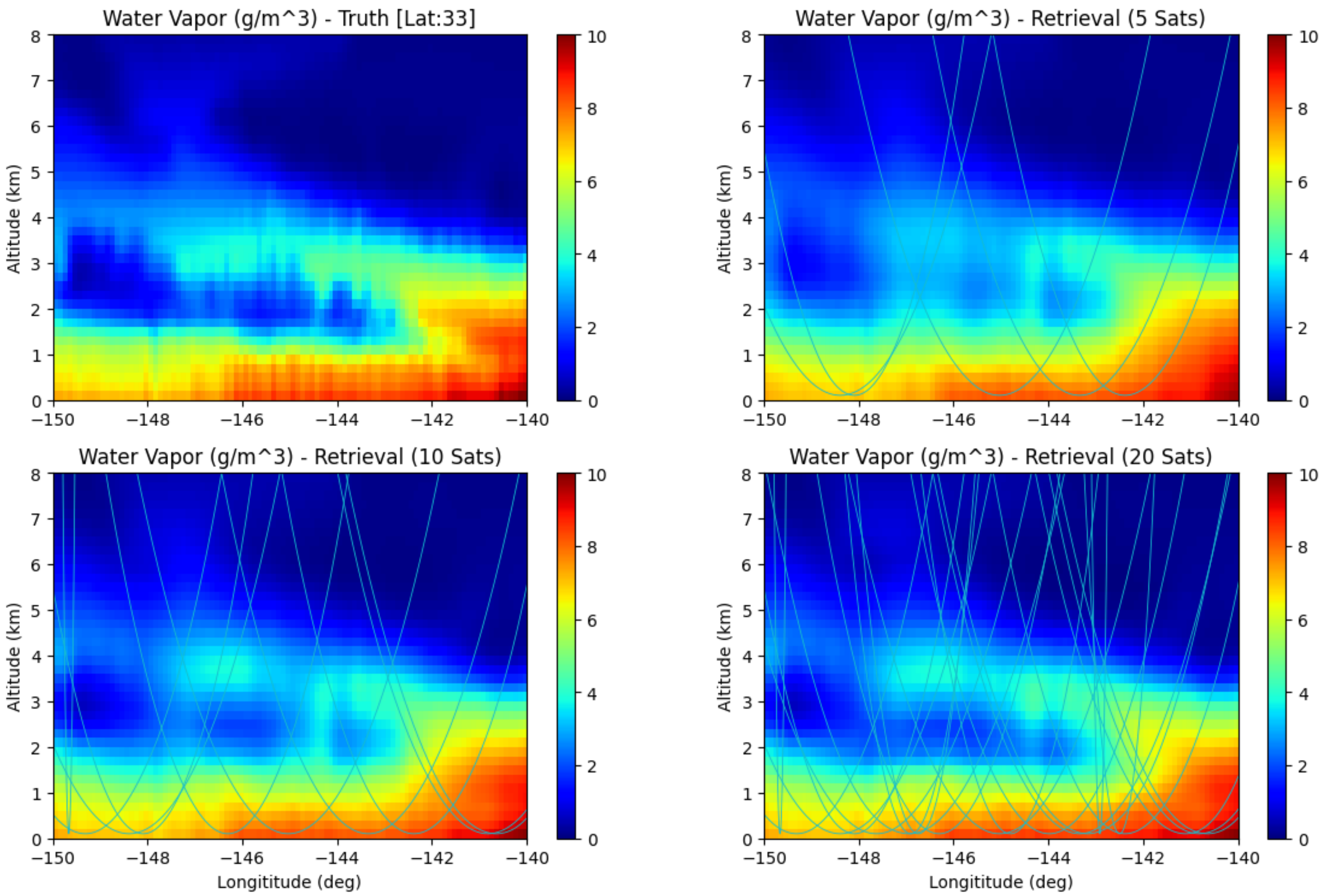

Figure 7. Upper-left: Vertical cross section showing water vapor of the WRF model at 33° latitude plane as truth. Upper-right: The tomography solution of water vapor with 5 ROs on the same plane. Each cyan solid curve corresponds to the lowest ray path of each RO projected on the plane. Lower-left: Same as upper-right panel but with 10 ROs. Lower-right: Same as lower-left panel but with 20 ROs.

point projected onto the 33° latitude plane. Since these are projections from randomly oriented planes in 3D onto the 33° plane, the concave size of each parabolic curve will vary depending on the angle between the actual RO plane and the 33° plane. The dashed circles in each panel of Fig. 8 are centered around tangent point locations of the various ROs for each case, showing their spatial distribution.

As shown in the upper right panel of Fig. 7, the reconstructed structure from 5 ROs remains mostly similar to the a priori (shown in the upper-right panel of Fig. 4). The retrieval does not detect the rapid changes around the edge of the tongue, a feature that is captured better in the case shown in the lower-right panel of Fig. 4. This is mainly due to the fact that the RO planes are not aligned with the 33° latitude plane near their tangent points, unlike the 2D geometry case studied in the previous subsection. But when more ROs are added to the 3D domain, the intrusion structure starts to emerge. The moisture gap at 2km height can be easily seen when 10 and 20 ROs (lower panels) are available. The impact of the RO locations can also be

https://doi.org/10.5194/egusphere-2026-4427
Preprint. Discussion started: 11 August 2026

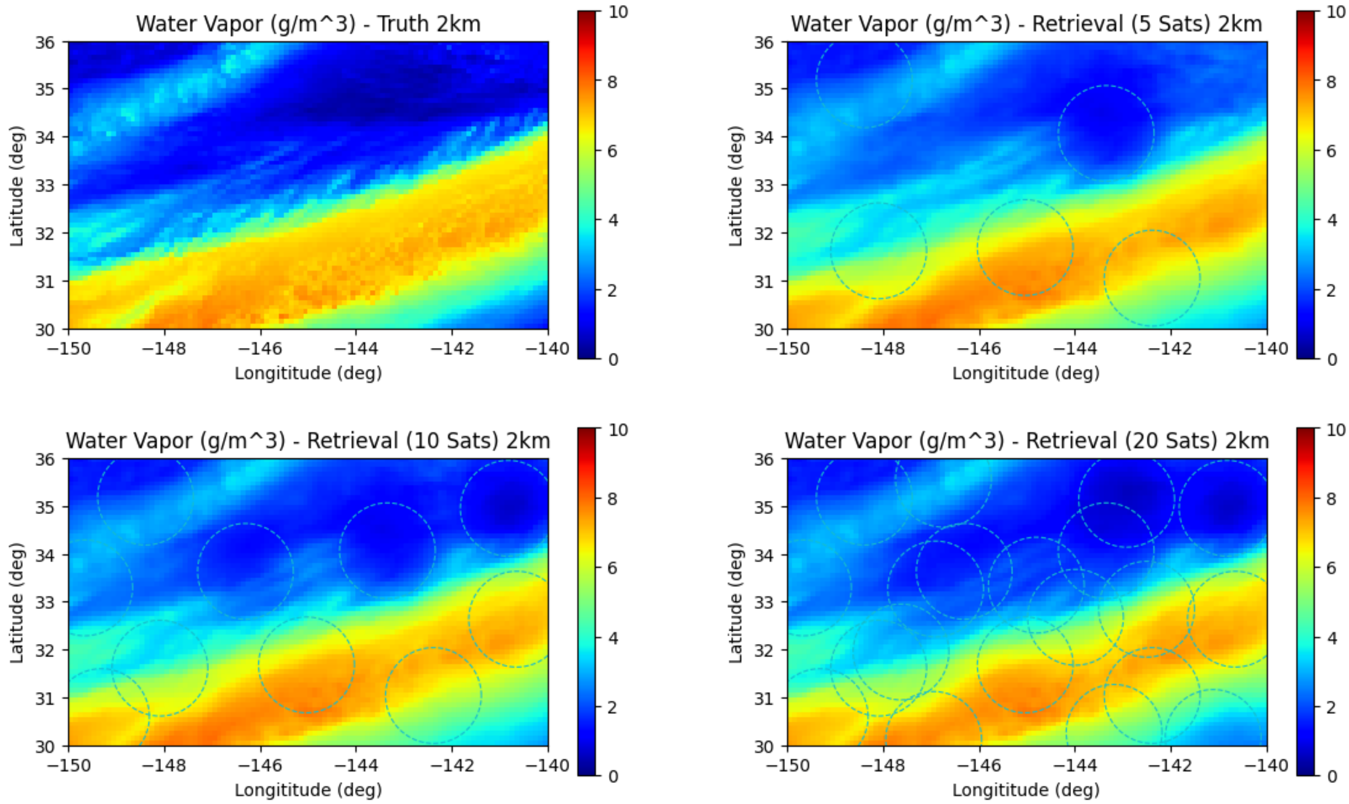

Figure 8. Same as Fig. 7 but on a horizontal plane at 2km. The dashed circles represent the circle of influence for each RO.

observed in the figure: the "bulge" structure between -148 and -146° longitudes between 2 to 4 km is seen in the upper-right panel due to no occultation present in that region. The structure disappears when more ray paths pass through the same region when 20 ROs are available (lower-right panel). Similar observations can also be made in the horizontal cross section at 2 km heights. Due to the lack of RO at the NE corner when only 5 ROs are available (upper-right panel in Fig. 8), the solution yields high water vapor value inherited from the a priori. But with more ROs cutting through that area, the vapor estimation shows significant reduction in the NE corner which matches better with the truth shown in the upper-left panel. Similar results can be observed between -148 and -144° longitudes around 32.5° latitude, where the vapor concentration was reduced and agrees better with the truth in the 10 and 20 RO cases compared to the 5 RO case where no RO ray path goes through that region. The improvement with the higher number of ROs in the 3D domain can also be quantified: Without RO, the RMSE of the nadir-retrieval solution is 0.428 g/m^3. With the presence of 5, 10, and 20 GNSS-RO cases the RMSE are reduced to 0.387 g/m^3, 0.354 g/m^3, and 0.310 g/m^3 respectively. This RMSE is computed over the entire simulated domain. The decrease would be much more significant if the RMSE is restricted to the region inside the "circle of influence" of the ROs.

To validate the robustness of the algorithm, we apply it to a much smoother a priori as shown in Fig. 9. Instead of the boxcar approach, the a priori in this case is smoothed horizontally first, and vertically next which creates a much smoother field (shown

https://doi.org/10.5194/egusphere-2026-4427
Preprint. Discussion started: 11 August 2026

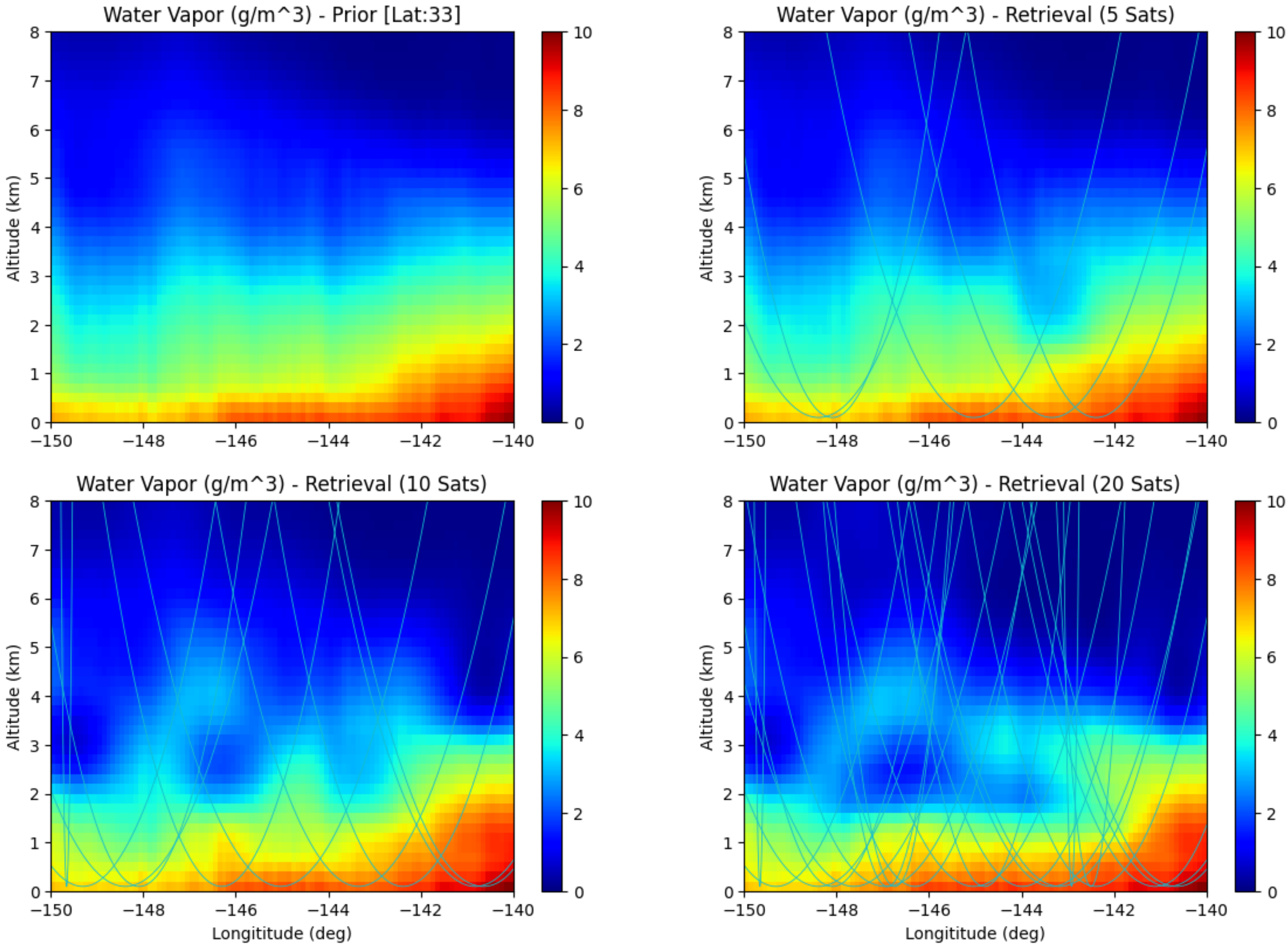

Figure 9. Same as Fig. 7 but with coarser smoothing of truth used as a priori. The vapor "hole" structure is revealed with sufficient number of ROs added in the tomography, even when the nadir retrieval is overly smoothed.

in the upper-left panel), where the vapor "hole" present in the true field is completely absent. The 20 GNSS-RO case shown in the lower right panel demonstrates that the complicated vertical moisture structure can still be recovered even when the a priori in this case provides little to no vertical information below 4 km height. While the 5 and 10 RO cases do not restore the structure on this vertical plane, these cases still provide the vertical information in regions close to the tangent points and reduce the error relative to the overly smoothed a priori. The RMSE of the overly-smoothed a priori is 1.09 g/m^3. With 5, 10 and 20 GNSS-RO added using the tomographic algorithm, the RMSE are reduced to 0.935 g/m^3, 0.803 g/m^3, and 0.616 g/m^3, respectively. The results show that the methodology can effectively combine the nadir and limb sounding observations and significantly improve the 3D solution, even when nadir retrieval is overly smoothed or biased.

https://doi.org/10.5194/egusphere-2026-4427
Preprint. Discussion started: 11 August 2026

3.2 COSMIC-2/ATMS observations

To demonstrate the applicability of the tomographic algorithm introduced in this paper with real RO and MWR observations, it was applied on a COSMIC-2/ATMS collocation case (2020-04-01-06:24c2f4_gps70). While multiple collocated GNSS-RO can be helpful to resolve the complicated 3D structures, as shown in the simulation results above, such occurrence is relatively rare with the current distribution of GNSS-RO observations. The case shown here is a single GNSS-RO collocated with MWR, which would be the most probable occurrence for GNSS-RO/MWR collocation. The geometry for this collocation and the corresponding ray path orientation is shown in Fig. 10. Located at the north coastline of Venezuela, the GNSS-RO ray paths, indicated by black solid lines, pass through both land and ocean within 0 to 8km altitude range. The tangent points (red dots) for each ray paths are located on the land area around [9.1N, 66.1W], while the MWR/IR footprint is uniformly distributed within 5° of the lowest tangent point location. The collocated Cross-track Infrared and Microwave Sounding Suite (CrIMSS) (Smith, 2019) derived temperature and water vapor dataset was interpolated to the 3D grid surrounding the tangent point location.

Vertical and horizontal cross sections of the interpolated 3D domain are shown in the upper and lower left panels in Fig. 11, respectively. The CrIMSS data shows that the atmosphere is generally moist (>10g/m3) below 3km on the west side of the domain and much drier between 1 to 3km height on the east side. While the air above 1.5 to 2km are dry on the east side of the domain, the cold, moist air beneath it collides with the warm air on the west and forms the weather front at around 63W longitude, presenting a complex vertical structure within the area. The right panels of Fig. 11 show the corresponding vertical and horizontal cross sections after combining the nadir and RO measurements. The combined tomographic solution reduces the vapor at ∼3km height close to the tangent point latitude (∼65° West), the lowest point of the cyan ray path, while increase the water content around 5km. The reduction extends to 2km height and makes the horizontal structure shown in the lower right panel close to the tangent point around [9N, 64W] much clearer. As expected, that the changes are mainly located around the tangent point because of the horizontal Hann window centered at the tangent point location.

The decaying influence of RO away from the tangent point due to the Hann window can be easily seen in the left panel of Fig. 12 which shows the difference between the retrieved and the a priori water vapor on the 9.28N latitude vertical plane. One can observe that outside of the window range of 2° radius the difference is zero (green color) at all altitudes, and negative and positive differences can be found at 3 and 5 km, respectively, near the tangent point location. The corresponding GNSS-RO refractivity retrieval and the a priori profile at the tangent point location (9.28N, -65.17W) are shown in the middle panel of Fig. 12, which shows that the RO refractivity profile is lower than the corresponding refractivity computed from the nadir observations between 1.5 to 4 km. This negative refractivity difference leads to smaller partial excess phase for ray paths located within this altitude range and contributes to the negative change in tomography retrieval seen in the left panel. Similarly, the positive bias in RO refractivity around 5km height leads to the positive change in the tomography retrieval shown in left panel. The green curve in the middle panel shows the tomography results at the tangent point location, which is close to the GNSS-RO solution capturing the small-scale vertical structure. This detailed refractivity structure is smoothed when the solutions are away from the tangent point, as shown in the right panel of Fig. 12. The dotted curves in color green and red are the profiles located at 1° east and west of the tangent point, respectively, and the corresponding a priori are shown as the dashed lines of

https://doi.org/10.5194/egusphere-2026-4427
Preprint. Discussion started: 11 August 2026

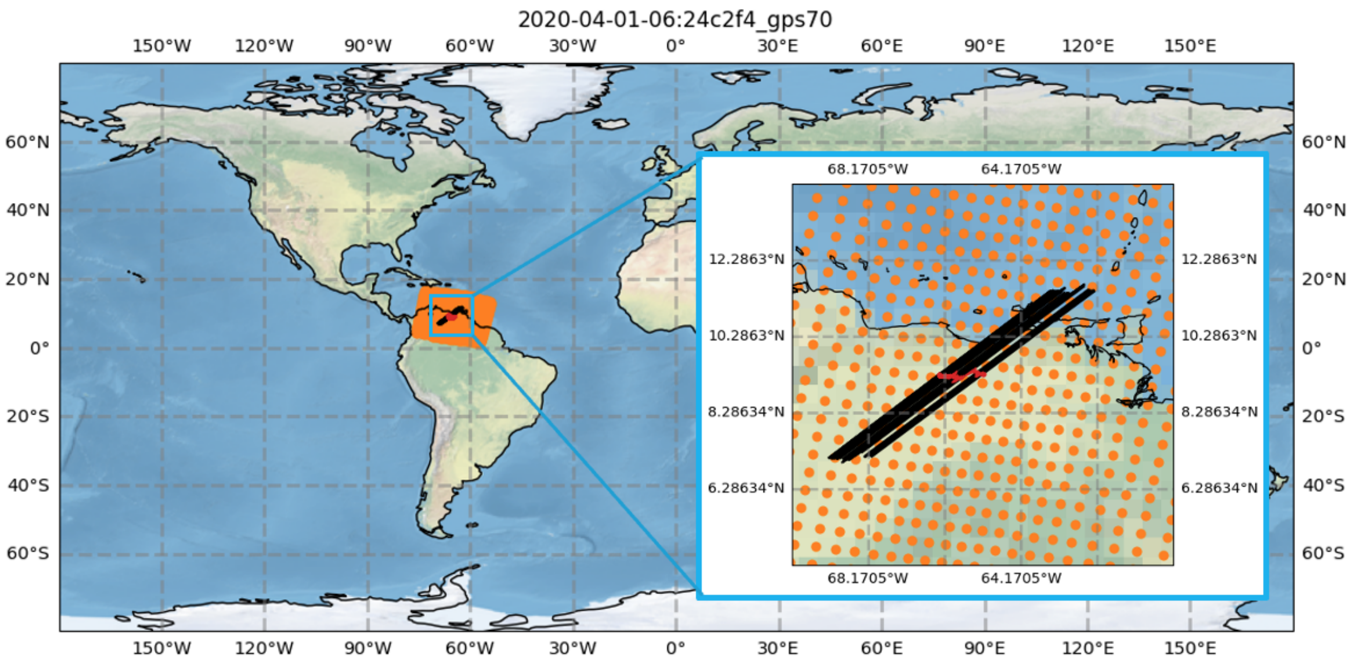

Figure 10. The collocation of GNSS-RO (2020-04-01-06:24c2f4_gps70) and CrIMSS dataset (SNDR.SNPP.CRIMSS.20200401TXXXX.m06.g0XX.L2_CLIMCAPS_RET_NSR.std). GNSS-RO tangent point locations for the RO links are shown as red dots, and their corresponding ray paths are shown in black solid lines. The orange dots shown in the zoom-in panel are the footprints of the CrIMSS dataset.

the same color. While these two solutions do not show detailed vertical structure as the original RO profile, the large scale structure, such as the sharp transition at around 2.5 km, is still inherited from the RO observations.

To further understand the negative (at ∼3km) and positive (at ∼5km) local maxima seen in the left panel of Fig. 12, we examine horizontal cross sections of the water vapor at 3 and 5 km in the imaged region, which are shown in Fig. 13. By comparing the difference between left (a priori/MWR-derived field) and right (retrieved field) panels, we see that the water content was significantly reduced near to the tangent point location at 3 km, leaving a gap around 9° North while the moist regions on the west side was preserved. By contrast, the vapor amount increased at 5km near the tangent point location, generating a vertical hollow structure. This type of 3D structure can be resolved only by combining GNSS-RO with existing nadir observations because of the latter's coarse vertical resolution.

4 Conclusions

In this article we introduced a new algorithm to take full advantage of collocated spaceborne nadir (MWR in this article, but applicable to IR) and limb (GNSS-RO) soundings to better observe and characterize the lower troposphere. While these two

https://doi.org/10.5194/egusphere-2026-4427
Preprint. Discussion started: 11 August 2026

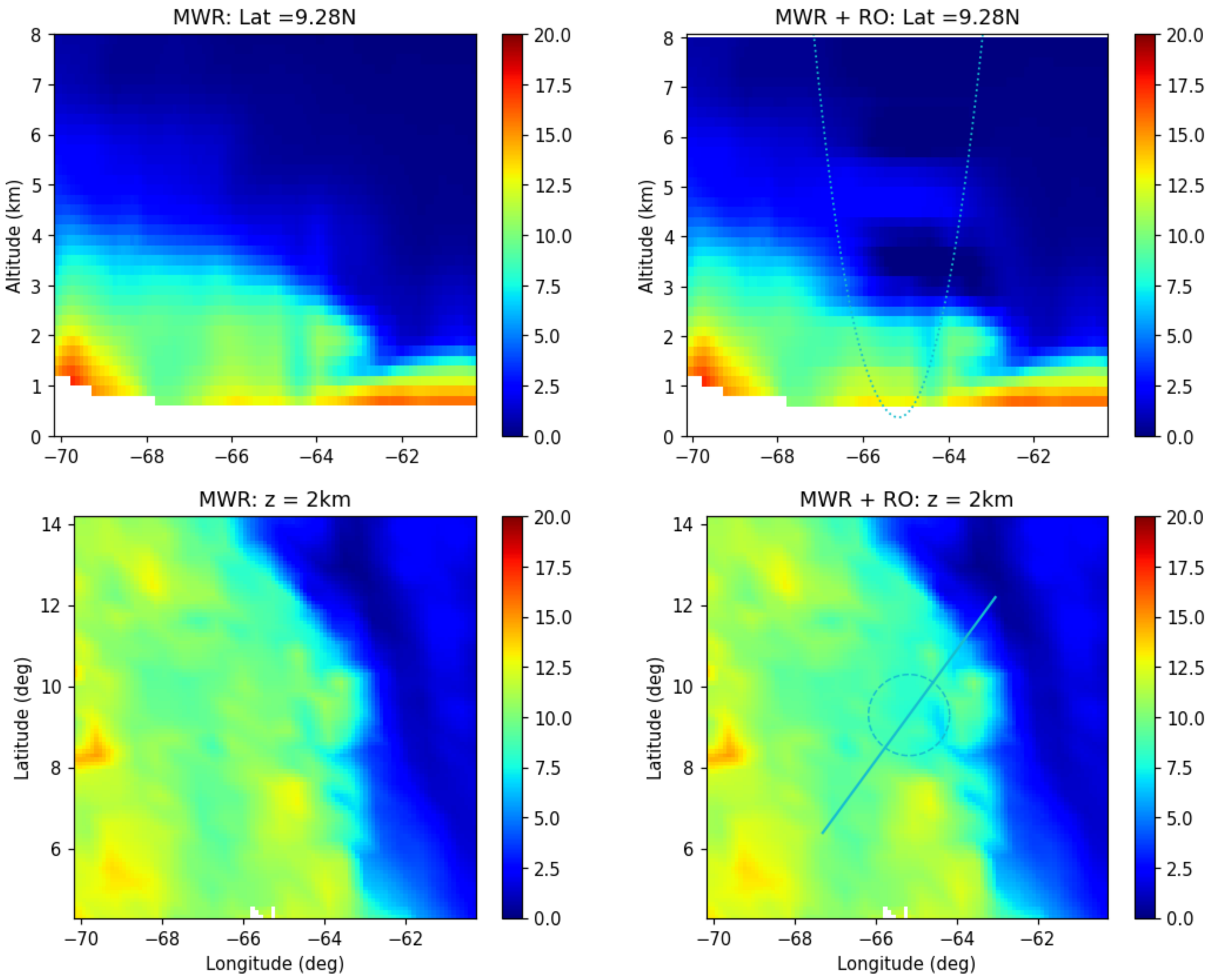

Figure 11. The water vapor domain comparison between a priori (nadir observation only, left) and the tomography retrieval (nadir + GNSS-RO, right). A vertical plane cross-section along the 9.28N latitude is shown in the top right panel. A horizontal plane cross-section at 2km height is shown in the lower. The solid line and the dashed cyan circle in the lower-right panel show the ray path of the lowest RO link and a circle of 1° radius centered at the tangent point

types of observations are complementary in many aspects, the algorithm introduced here focuses on the spatial resolution synergy between the two: nadir sounders provides high horizontal resolution (15 to 20 km) while limb soundings offer high vertical resolution (∼200m). To our knowledge, this is the first attempt to combine the two observations in a model-independent way to resolve the complex lower troposphere water vapor structures in 3D. While numerical weather prediction models have assimilated both passive nadir measurements and RO data, the current algorithm provides a more model-independent solution which can land further insight on optimal methods that could benefit data assimilation techniques. The tomographical framework introduced here combines temperature/water vapor profiles from nadir sounders at each footprint and partial excess

https://doi.org/10.5194/egusphere-2026-4427
Preprint. Discussion started: 11 August 2026

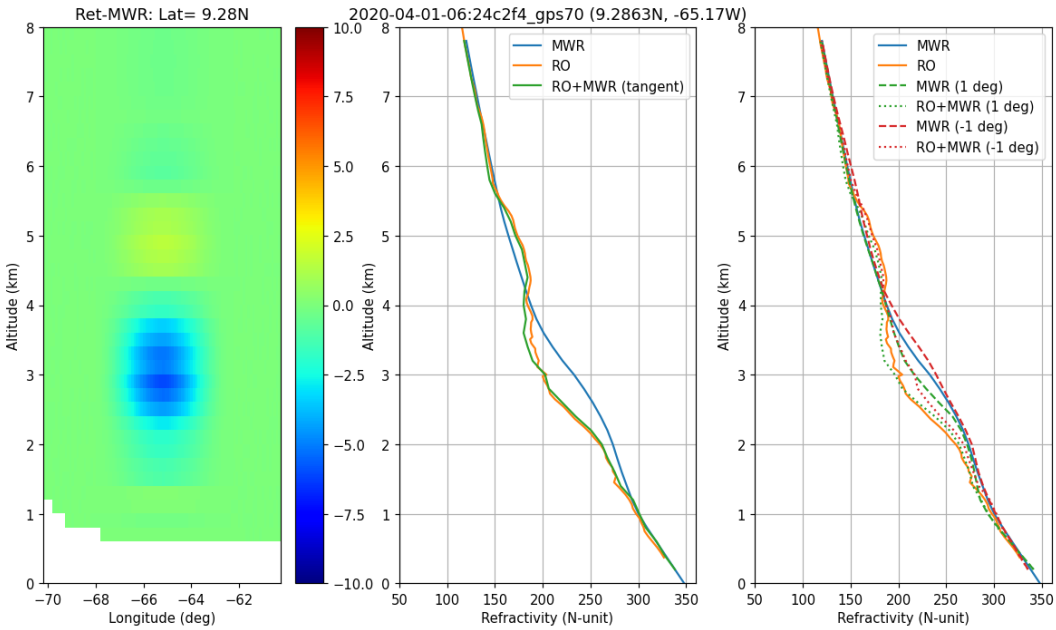

Figure 12. [Left panel] The water vapor difference between the tomographical retrieval and the a priori from nadir observations along the 9.28N latitude vertical plane. [Middle panel] The 1D refractivity profile from nadir observations at the GNSS-RO tangent point location (blue), GNSS-RO-only retrieval (orange), and the combined GNSS-RO/MWR tomography retrieval (green). [Right panel] Refractivity profiles from nadir observations at 1° east (green dashed) and west (red dashed) of the tangent point, and corresponding tomography solutions at 1° east (green dotted) and west (red dotted)

phase computed by use of GNSS-RO refractivity product and ray tracing. In this article, the developed algorithm was applied on numerous simulation scenarios including one or more GNSS-RO collocations, in 2D and 3D geometries. It was also tested with GNSS-RO/CRIMSS collocation measurements to demonstrate its applicability to real data.

The work presented here ignores systematic biases in RO derived refractivity and in passive sounders. Using the presented tomography framework in reality would have to account for these biases. The GNSS-RO refractivity observation could be negatively-biased at lower troposphere, which may cause negatively-biased vapor tomographic retrievals. This can be mitigated if RO bending measurements are used as the tomography input because these measurements will not experience biases due to atmospheric ducting. However, extracting bending within the lower troposphere from the raw observations can be challenging and needs to be further developed. Biases in passive sounders and other challenges caused by cloud and precipitation is a long-standing challenge that remains an active area of research. The tomography framework described here could further be improved by a careful consideration of the measurements error covariance as well the model representation error, an issue that we will leave for a future investigation.

https://doi.org/10.5194/egusphere-2026-4427
Preprint. Discussion started: 11 August 2026

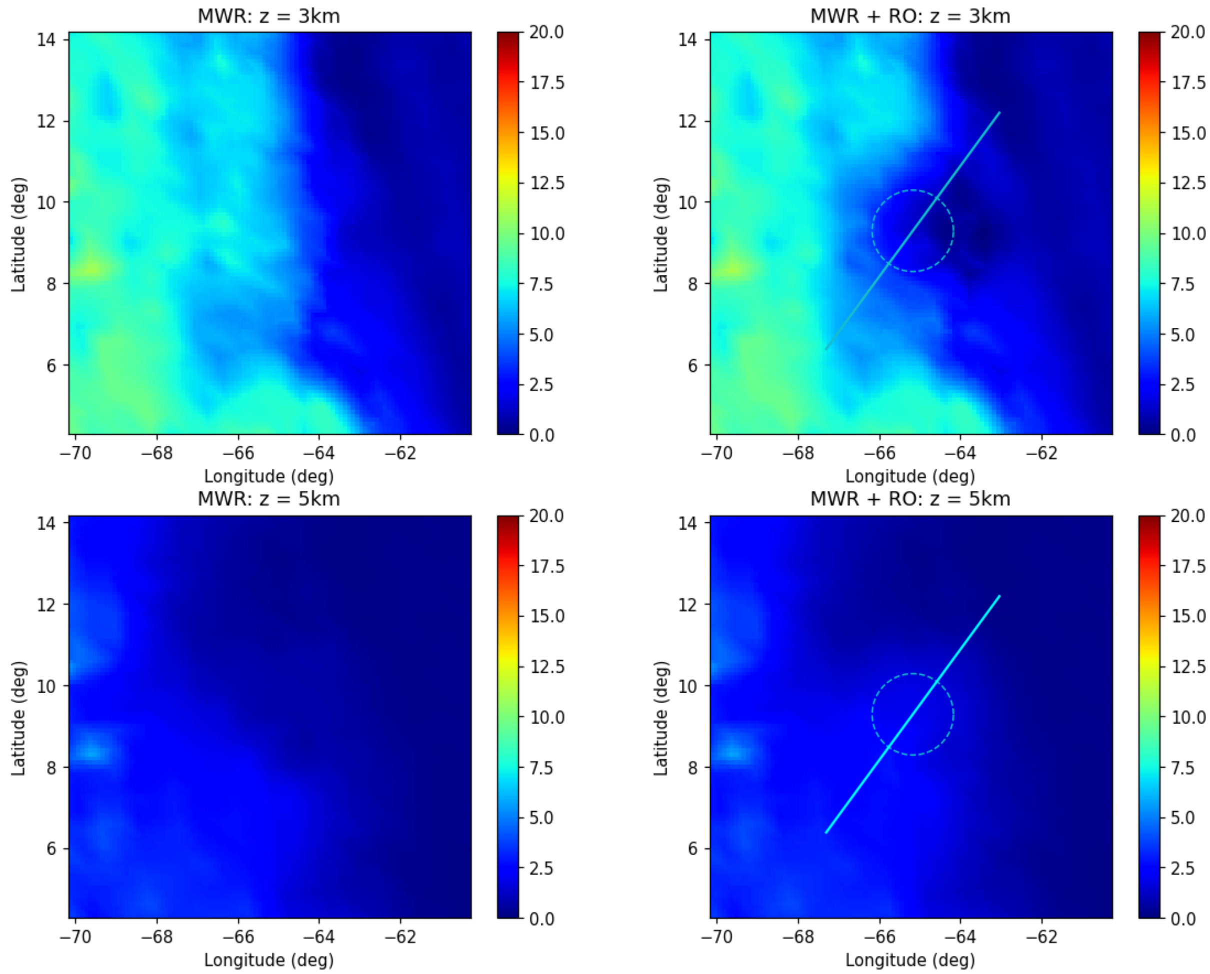

Figure 13. Same as Fig. 11 but for the horizontal planes at 3km (upper-panel) and 5km (lower-panel). The cyan solid lines are the GNSS-RO ray path and the dashed circles are the 1° circle centered at the tangent point.

Appendix A: 2D ray tracing

Here we give a brief description of the 2D ray tracing described in Radio Occultation Processing Package (ROPP) (ROPP
415 document, 2020) (Culverwell et al., 2015). The height of each point on a specific ray path z^{rp} can be described by a differential equation as:

$$\frac{dz^{rp}}{ds} = \cos(\sigma) \tag{A1}$$

where s is the distance along the ray path from the tangent point, and σ is the angle between the radial vector and ray path tangent vector (shown as the orange dashed line in Fig. A1) at each point.

https://doi.org/10.5194/egusphere-2026-4427
Preprint. Discussion started: 11 August 2026

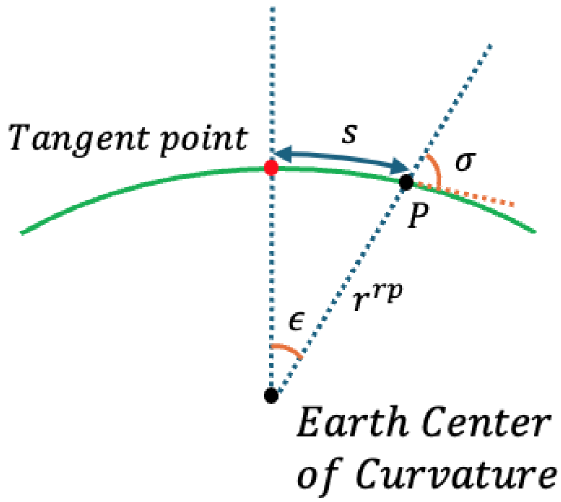

Figure A1. Illustration of the 2D ray tracing for the variables used in Eq. A1 to Eq. A4. Point P is an arbitrary point on the ray path shown as the green solid line. All the variables are defined in the texts.

The distance from local center of curvature to each point on the ray path can then be easily calculated:

$$r^{rp} = z^{rp} + R_c \tag{A2}$$

where R_c is the radius of curvature. In addition, we define the angle ϵ as the horizontal angular position of each point along the ray path with respect to the tangent point:

$$\frac{d\epsilon}{ds} = \frac{\sin(\sigma)}{r^{rp}} \tag{A3}$$

The angle σ itself can also be derived from a differential equation that is linked to the known refractivity field:

$$\frac{d\sigma}{ds} = -\sin(\sigma)\left[\frac{1}{r^{rp}} + \left(\frac{\partial n}{\partial r}\right)_\epsilon\right] \tag{A4}$$

where $\left(\frac{\partial n}{\partial r}\right)_\epsilon$ is the derivative of refractive index with respect to height at a specific point in the ray path with the horizontal angle ϵ. This can be achieved by interpolating the vertical refractivity gradient calculated from the atmospheric column where the specific point in the ray path located within the 3D domain. Notice that the horizontal refractivity gradient is not considered, since its impact to the limb ray path is very limited and neglecting it can largely reduce the computational burden. By simultaneously solving these three variables from Eq. A1, A3, and A4 using the Runge-Kutta (RK4) method, the position of each point in the ray path can be obtained, and the corresponding latitude, longitude and height can be calculated. The described 2D ray tracing process is initialized at the tangent point, where $\sigma_{tp} = \pi/2$ and $\epsilon_{tp} = 0$, and propagated on both sides along the occultation plane until the edge of the 3D domain.

https://doi.org/10.5194/egusphere-2026-4427
Preprint. Discussion started: 11 August 2026

Code and data availability. The GNSS-RO and MWR satellite data used in this study are available from UCAR CDAAC (https://doi.org/10.5065/t353-c093) and NASA GESDISC (https://doi.org/10.5067/KU5L6AXRNQX8), respectively. The tomography algorithm and processing code written in Python is under release review and only available on request.

Author contributions. KNW, COA, and GAH conceptualized the method. KNW developed the methodology and performed the analysis and validation. KNW implemented the software, and COA supervised the project. KNW, GAH, and COA wrote the manuscript. All authors reviewed the final article.

Competing interests. The contact author has declared that none of the authors has any competing interests.

Disclaimer.

Acknowledgements. The research described in this paper was carried out at the Jet Propulsion Laboratory (JPL), California Institute of Technology, under a contract with the National Aeronautics and Space Administration. It is funded by the NASA grant NNH24ZDA001N-DSI. We would also like to thank Svetla Hristova-Veleva from JPL for providing WRF simulation results for this study.

https://doi.org/10.5194/egusphere-2026-4427
Preprint. Discussion started: 11 August 2026

References

Ao, C. O. *Effect of ducting on radio occultation measurements: an assessment based on high-resolution radiosonde soundings*, Radio Sci., 42, RS2008, https://doi.org/10.1029/2006RS003485, 2007.

Bao, Y., J. Xu, A. M. Powell Jr., M. Shao, J. Min, and Y. Pan, *Impacts of AMSU-A, MHS and IASI data assimilation on temperature and humidity forecasts with GSI–WRF over the western United States*, Atmos. Meas. Tech., 8, 4231–4242, https://doi.org/10.5194/amt-8-4231-2015, 2015.

Barnet, C. (2019), Sounder SIPS: Suomi NPP CrIMSS Level 2 CLIMCAPS Normal Spectral Resolution: Atmosphere cloud and surface geophysical state V2, Greenbelt, MD, USA, Goddard Earth Sciences Data and Information Services Center (GES DISC), 10.5067/9HR0XHCH3IGS

Borbás, É., W. P. Menzel, J. Li, and H. M. Woolf, *Combining radio occultation refractivities and IR/MW radiances to derive temperature and moisture profiles: A simulation study plus early results using CHAMP and ATOVS*, J. Geophys. Res., 108, 4676, doi:10.1029/2003JD003386, D21, 2003.

Bormann, N., A. Fouilloux, and W. Bell, *Evaluation and assimilation of ATMS data in the ECMWF system*, J. Geophys. Res. Atmos., 118, 12,970– 12,980, doi:10.1002/2013JD020325, 2013.

Boukabara, S.-A., K. Garrett, W. Chen, F. Iturbide-Sanchez, C. Grassotti, C. Kongoli, R. Chen, Q. Liu, B. Yan, F. Weng, R. Ferraro, T. J. Kleespies, and H. Meng, *MiRS: An All-Weather 1DVAR Satellite Data Assimilation and Retrieval System* IEEE Transactions on Geoscience and Remote Sensing, 49, 9, 3249-3272, doi: 10.1109/TGRS.2011.2158438, 2011.

Collard, A. D. and S. B. Healy, *The combined impact of future space-based atmospheric sounding instruments on numerical weather-prediction analysis fields: A simulation study.* Q.J.R. Meteorol. Soc., 129: 2741-2760. https://doi.org/10.1256/qj.02.124, 2003.

Culverwell, I. D., Lewis, H. W., Offiler, D., Marquardt, C., and Burrows, C. P.: The Radio Occultation Processing Package, ROPP, Atmos. Meas. Tech., 8, 1887–1899, https://doi.org/10.5194/amt-8-1887-2015, 2015.

EUMETSAT, ROMSAF, *ROPP Forward Model module User Guide, V.10*, https://www.romsaf.org/ropp/, 2020.

Fujita, M. and T. Sato, *Observed behaviours of precipitable water vapour and precipitation intensity in response to upper air profiles estimated from surface air temperature.* Sci Rep 7, 4233. https://doi.org/10.1038/s41598-017-04443-9, 2017.

Gorbunov, M. E., V. V. Vorob'ev, and K. B. Lauritsen, *Fluctuations of refractivity as a systematic error source in radio occultations*, Radio Sci., 50, 656–669, doi:10.1002/2014RS005639, 2015.

Hajj, G. A., R. Ibañez-Meier, E. R. Kursinski, and L. J. Romans, *Imaging the ionosphere with the global positioning system* Int. J. Imaging Syst. Technol., 5: 174-187. https://doi.org/10.1002/ima.1850050214, 1994.

Hajj, G. A., E. R. Kursinski, L. J. Romans, W. I. Bertiger, and S. S. Leroy. *A technical description of atmospheric sounding by GPS occultation* Journal of Atmospheric and solar-terrestrial physics 64, 4:451-469, 2002.

Ho, S., Y. Kuo, and S. Sokolovskiy, *Improvement of the Temperature and Moisture Retrievals in the Lower Troposphere Using AIRS and GPS Radio Occultation Measurements.* Journal of Atmospheric and Oceanic Technology, 24(10), 1726-1739, 2007.

Holloway, C. E. and J. D. Neelin, *Moisture Vertical Structure, Column Water Vapor, and Tropical Deep Convection*, Journal of the Atmospheric Sciences, 66(6), 1665-1683, 2009.

Kazumori, M., Q. Liu, R. Treadon, and J. C. Derber, *Impact Study of AMSR-E Radiances in the NCEP Global Data Assimilation System*, Monthly Weather Review, 136(2), 541-559. https://doi.org/10.1175/2007MWR2147.1, 2008.

https://doi.org/10.5194/egusphere-2026-4427
Preprint. Discussion started: 11 August 2026

Kursinski, E. R., G. A. Hajj, J. T. Schofield, R. P. Linfield, and K. R. Hardy, *Observing Earth's atmosphere with radio occultation measurements using the Global Positioning System.* Journal of Geophysical Research 102, 23 429-23 466, 1997

Moeller, G., Ao, C. O., and Mannucci, A. J., *Tomographic radio occultation methods applied to a dense cubesat formation in low Mars orbit* Radio Science, 56, e2020RS007199. https://doi.org/10.1029/2020RS007199

Mülmenstädt, J., M. Salzmann, and J. E. Kay. *An underestimated negative cloud feedback from cloud lifetime changes* Nat. Clim. Chang. 11, 508–513 (2021). https://doi.org/10.1038/s41558-021-01038-1, 2021.

Rodgers, C. D., *Inverse Methods for Atmospheric Sounding - Theory and Practice*, World Scientific Publishing Co. Pte. Ltd., ISBN: 9789812813718, doi:10.1142/9789812813718, 2000.

Sherwood, S. C., R. Roca, T. M. Weckwerth, and N. G. Andronova, *Tropospheric Water Vapor, Convection, and Climate*, Rev. Geophys., 48, RG2001, doi:10.1029/2009RG000301, 2010.

Syndergaard, Stig, E. Robert Kursinski, Benjamin M. Herman, Emily M. Lane, and David E. Flittner. *A refractive index mapping operator for assimilation of occultation data*, Monthly weather review 133, no. 9, 2650-2668, 2005.

Smith, E. K., and S. Weintraub (1953), *The constants in the equation for atmosphere refractive index at radio frequencies*, Proc. IRE, 41, 1035–1037, 1953.

Stevens, B., H. Brogniez, C. Kiemle, J.-L. Lacour, C. Crevoisier and J. Kiliani, *Structure and Dynamical Influence of Water Vapor in the Lower Tropical Troposphere.* Surv Geophys 38, 1371–1397, https://doi.org/10.1007/s10712-017-9420-8, 2017.

Teixeira, J., J. R. Piepmeier, A. R. Nehrir, C. O. Ao, S. S. Chen, C. A. Clayson, A. M. Fridlind, M. Lebsock, W. McCarty, H. Salmun, J. A. Santanello, D. D. Turner, Z. Wang, and X. Zeng, *Toward a Global Planetary Boundary Layer Observing System: The NASA PBL Incubation Study Team Report.* NASA PBL Incubation Study Team. 134 pp.

Wulfmeyer, V., R. M. Hardesty, D. D. Turner, A. Behrendt, M. P. Cadeddu, P. Di Girolamo, P. Schlüssel, J. Van Baelen, and F. Zus, *A review of the remote sensing of lower tropospheric thermodynamic profiles and its indispensable role for the understanding and the simulation of water and energy cycles*, Rev. Geophys., 53, 819–895, doi:10.1002/2014RG000476.

Wang, K.-N., J. L. Garrison, U. Acikoz, J. S. Haase, B, J. Murphy, P. Muradyan, T. Lulich, *Open-Loop Tracking of Rising and Setting GPS Radio-Occultation Signals From an Airborne Platform: Signal Model and Error Analysis* IEEE Transactions on Geoscience and Remote Sensing, 54, no. 7, 3967-3984, doi: 10.1109/TGRS.2016.2532346, 2016.

Wang, K.-N., M. de la Torre Juárez, C. O. Ao, and F. Xie (2017), *Correcting negatively biased refractivity below ducts in GNSS radio occultation: an optimal estimation approach towards improving planetary boundary layer (PBL) characterization.* Atmos. Meas. Tech., 10, 4761–4776, https://doi.org/10.5194/amt-10-4761-2017, 2017.

Wang, K.-N., Ao, C. O., Morris, M. G., Hajj, G. A., Kurowski, M. J., Turk, F. J., and Moore, A. W (2024), *Joint 1DVar retrievals of tropospheric temperature and water vapor from Global Navigation Satellite System radio occultation (GNSS-RO) and microwave radiometer observations.* Atmos. Meas. Tech., 17, 583–599, https://doi.org/10.5194/amt-17-583-2024, 2024.

Xie, F., S. Syndergaard, E. R. Kursinski, and B. M., Herman(2006), *An approach for retrieving marine boundary layer refractivity from GPS occultation data in the presence of superrefraction.* J. At- mos. Ocean. Tech., 23, 1629–1644, 2006.

Zhou, C., M. Zelinka and S. Klein, Impact of decadal cloud variations on the Earth's energy budget. Nature Geosci 9, 871–874. https://doi.org/10.1038/ngeo2828, 2016.